Article



# Optimizing FDM Printing Parameters to Reduce Deformation in Annealed HTPLA Patient-Specific Instruments

Leonardo Frizziero , Grazia Chiara Menozzi * , Andrea Montalti , Giulia Alessandri , Paola Papaleo , Giovanni Trisolino , Gino Rocca

Posted Date: 3 November 2025

doi: 10.20944/preprints202511.0067.v1

Keywords: FDM; 3D printing; additive manufacturing; patient-specific instrument; annealing; orthopedics

 doi:10.20944/preprints202511.0067.v1



*Article*

# Optimizing FDM Printing Parameters to Reduce Deformation in Annealed HTPLA Patient-Specific Instruments

**Leonardo Frizziero [1], Grazia Chiara Menozzi [2,*], Andrea Montalti [1], Giulia Alessandri [2], Paola Papaleo [1], Giovanni Trisolino [2] and Gino Rocca [2]**

[1] Department of Industrial Engineering, Alma Mater Studiorum University of Bologna, 40136 Bologna, Italy

[2] Unit of Pediatric Orthopedics and Traumatology, IRCCS Istituto Ortopedico Rizzoli, 40136 Bologna, Italy

* Correspondence: graziachiara.menozzi@ior.it

**Abstract**

Computer-Aided Design (CAD) and Additive Manufacturing (AM), particularly Fused Deposition Modelling (FDM) with PLA, are increasingly used in medicine for cost-effective production of sterilizable patient-specific instruments (PSIs). This study investigates which printing parameters most influence deformation after annealing, a key pre-sterilization step, to identify optimal 3D printing settings that minimize geometric distortion. Experiments were conducted using $2^4$ factorial design to evaluate the effects of raft thickness, infill orientation, first-layer pattern, and cooling fan speed on three-dimensional deformation and deformation on plane A, parallel to the printing plane, and plane B, longitudinal to the specimen, then projected in a $2^3$ design with replicates. Lower fan speed (25%) and a 45° infill orientation minimized overall deformation, while a 90° orientation reduced distortion on Plane A. Results varied across planes, likely due to the anisotropic nature of FDM parts. Despite limitations, this study provides a first insight into deformation behavior in larger PSIs and supports future optimization efforts.

**Keywords:** FDM; 3D printing; additive manufacturing; patient-specific instrument; annealing; orthopedics

## 1. Introduction

Computer-Aided Design (CAD) is a digital representation tool that supports the creation, development, and revision of designs. Thanks to its versatility, CAD is well suited for multidisciplinary projects, allowing data integration and process optimization across different domains [1]. One of the earliest applications of CAD technology in medicine was introduced in the mid-1980s by Vannier et al., who used it for craniofacial surgical planning and evaluation based on surface contours derived from CT scans [2].

Additive manufacturing (AM), or 3D printing, creates objects layer by layer directly from digital models. First introduced in the 1980s with stereolithography (SLA) by Chuck Hull [3], AM has since expanded with techniques and materials that allow high precision, design flexibility, and complex geometries. Initially used for rapid prototyping [4], it is now applied across aerospace, automotive, fashion, and medicine [5–10]. Among the most widespread methods is fused deposition modelling (FDM), valued for its low costs and ability to process a wide range of thermoplastics such as Acrylonitrile-Butadiene-Styrene (ABS) and Polylactic Acid (PLA) [11–13].

PLA is a semicrystalline biopolymer used from biodegradable packaging to medical implants. In healthcare, AM enables cost-effective production of prosthetics, implants, dental devices, and anatomical models, and more recently has supported Patient-Specific Instruments (PSIs), such as surgical guides, and implants to improve precision and personalization [9,14,15].

 doi:10.20944/preprints202511.0067.v1



In FDM, rapid heating, extrusion, and cooling lead to internal stresses, shrinkage, weak interlayer adhesion, and voids that can compromise part quality [16,17]. Annealing is an effective post-processing technique that increases crystallinity, relieves stresses, improves adhesion, and enhances mechanical performance, though it can also alter dimensional tolerances, requiring shrinkage and expansion to be considered during design [18]. Printing parameters strongly influence deformation in AM, and statistical optimization methods are often used to control variability. Donnici et al., for instance, used RSM to optimize lattice stiffness in AM [19].

In medical applications, steam sterilization (121–134 °C) presents further challenges, as material like PLA softens above its glass transition. Nevertheless, studies indicate that with proper conditioning, such as material selection, geometric design, and pre-annealing, PLA can better withstand autoclaving, showing reduced deformation and adequate strength.

The PSI analysed in this experiment was a cutting guide previously designed for a bone resection procedure. It was chosen due to its notably large dimensions, which is an uncommon characteristic in pediatric orthopedics, where guides are typically smaller and, to date, have not shown significant deformation. The increased length of the guide resulted in substantial warping, prompting a more in-depth investigation aimed at identifying optimal printing parameters to ensure reproducible and reliable outcomes, even for larger geometries.

The aim of this study is to investigate the effect of printing parameters on the deformation of PSIs after 3D printing and annealing, with the goal of identifying the optimal parameter combination that minimizes geometric deviation from the original CAD model.

## 2. Materials and Methods

This experiment was conducted based on the current manufacturing process, as defined in previous studies [20,21]. The aim was to investigate additional parameters whose influence on deformation is not yet fully understood, to identify which printing parameters most significantly affect the final deformation of PSIs following thermal annealing prior to sterilization.

### *2.1. The Manufacturing Process and Printing Setup*

To date, PSIs have always been manufactured and annealed according to a process which has been defined in previous studies (Figure 1). The manufacturing process begins with the design of the cutting guide using CAD software (Creo Parametric). The resulting 3D model is exported in STL format and imported into the slicing software (Bambu Studio), where it is oriented on the print bed and the printing parameters are defined. The model is then 3D printed in HTPLA, after which the cutting guides are annealed according to a thermal cycle and subsequently sent for sterilization. The selection of the material and the definition of the thermal treatment process were established in previous studies [20,22,23].

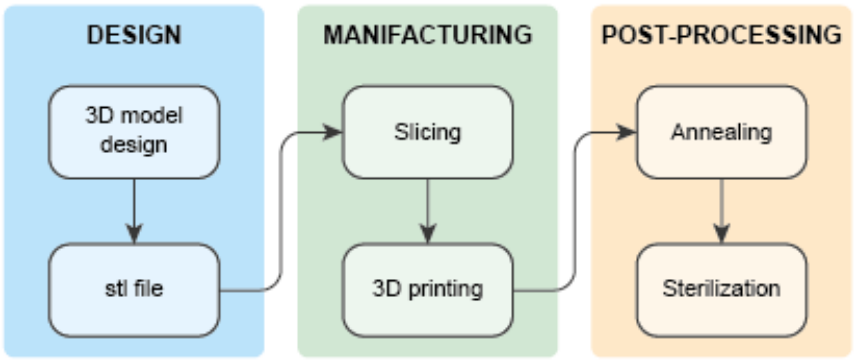


**Figure 1.** Standard designing and printing process.

 doi:10.20944/preprints202511.0067.v1



Some predefined key printing parameters (Table 1) and the time and temperature required for annealing (Table 2) were kept constant throughout the study. The properties of the HTPLA material used are summarized in Table 3.

**Table 1.** Unchanged basic printing parameters.

| Parameter | Value |
|---|---|
| Nozzle width | 0.4 mm |
| Layer height | 0.2 mm |
| Infill | 100% |
| Infill pattern | Monotonic |
| Infill overlap percentage | 20% |
| Wall loops | 3 |
| Nozzle temperature | 220 °C |
| Bed temperature | 60 °C |

**Table 2.** Temperature and time cycle for the annealing process.

| Phase[1] | Time (minutes) | Temperature (°C) |
|---|---|---|
| 1st | 10 | 80 |
| 2nd | 40 | 100 |

[1] The treatment is performed in a single cycle with two thermal phases.

**Table 3.** Main Properties of HTPLA (PLA Crystal Clear, Fillamentum Manufacturing Czech).

| PLA Crystal Clear | | |
|---|---|---|
| Thermal properties | Glass transition temperature | 55-60 °C |
| | Melting point | 150-230 °C |
| | Decomposition temperature | >230 °C |
| Printing properties | Print temperature | 210-230 °C |
| | Hot pad | 50-60 °C |
| Physical Properties | Material density | 1.24 g/cm$^3$ |
| Mechanical properties | Tensile strength | 50 MPa |

*2.2. Design Features and Positioning on the Print Bed*

The cutting guide used in this experiment was selected due to its large dimensions with a length of 142 mm. The basic printing parameters previously described, as well as the guide's orientation on the print bed, were kept consistent across all samples. The guide featured lateral extensions designed for support and bone contact, connected by a central rod (Figure 2a). It was positioned centrally on the print bed with its largest flat surface facing downward. This orientation, defined during the design phase, ensures that the bone-contacting surface faces upward, thus eliminating the need for support structures and minimizing the risk of dimensional inaccuracies (Figure 2b).

 doi:10.20944/preprints202511.0067.v1



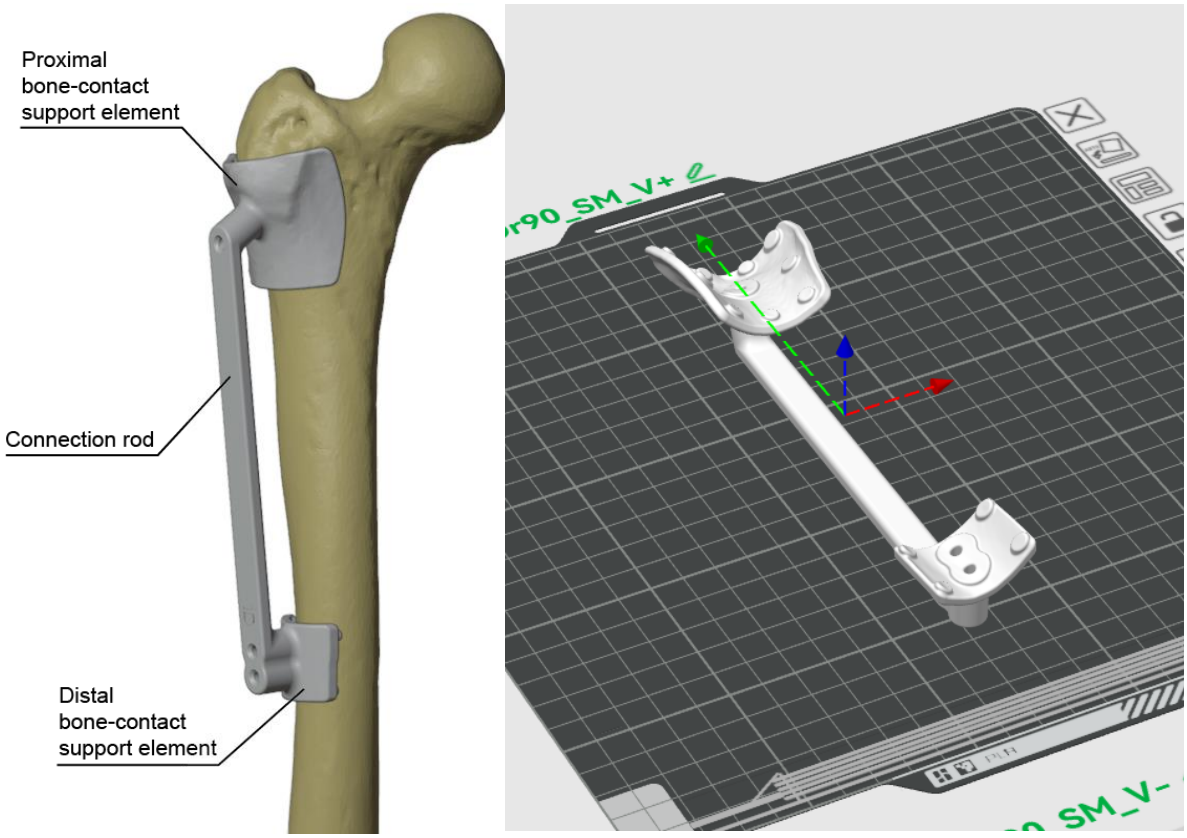


(**a**) (**b**)

**Figure 2.** The cutting guide selected for the experiment based on its geometry. (**a**) Cutting guide and its features; (**b**) Print bed orientation of the cutting guide, designed to prevent the use of support structures on the bone-contacting surface, the arrow represents the reference system x, y and z (red, green and blue respectively).

*2.3. The Design of the Experiment*

This experiment was conducted using a factorial design because of the high number of factors to be investigated. Based on literature findings on parameters influencing internal stresses in FDM printing [24–26], four factors were selected and tested at two levels ("high" and "low") for investigation: raft thickness, infill pattern orientation, first-layer surface pattern, and cooling fan speed.

1. Raft thickness was included as it is hypothesized to act as a mechanical constraint during annealing, to preserve the geometry by resisting deformation. Two conditions were tested: 0 layers (absence of raft) and 6 layers (presence of raft), considered as categorical levels;
2. Infill pattern orientation was selected based on the assumption that different internal geometries influence the distribution of residual stresses during cooling. These stresses are later released during annealing, potentially affecting the final shape. Two orientations were tested: 90° and 45° relative to the longitudinal axis of the cutting guide;
3. First-layer pattern was included to evaluate whether changing the default monotonic infill to a slower, more intricate deposition path (Hilbert curve) affects residual stress accumulation;
4. Fan speed was varied to assess its impact on the cooling rate during deposition, which in turn may influence internal stresses. Two levels were defined: 100% and 25% fan power.

The experiment was designed as a $2^4$ factorial experiment and the runs factors and levels are summarized in Table 4.

**Table 4.** Values of the high and low levels for each factor.

| | Factor | Levels | |
|---|---|---|---|
| | | Low (-) | High (+) |
| Raft thickness (layers) | A | 0 | 6 |

 doi:10.20944/preprints202511.0067.v1



| | | | |
|---|---|---|---|
| Infill pattern angle (°) | B | 45° | 90° |
| First-layer pattern (type) | C | M (Monotonic) | H (Hilbert curve) |
| Fan speed (%) | D | 25% | 100% |

*2.4. Measurements*

The experiment was carried out by comparing the values of the original CAD model with those of the specimens treated prior to sterilization. All specimens were 3D printed using the Bambu Lab X1 Carbon printer (Shenzhen, China) following the randomized order defined by the experimental design. They were then subjected to the annealing process described above. After thermal treatment, the specimens were cleaned from all supports (Figure 3) and scanned using a FARO Quantum S arm in combination with Geomagic Design X to generate STL files for each sample. These files were subsequently analyzed by comparing them to the original CAD model.

Deformation analysis was conducted using 3D distance maps between the original CAD model and the STL files of the 3D-printed specimens (Figure 4), as well as by evaluating 2D cross-sections along predefined planes: plane A, parallel to the printing bed intersecting the connecting rod (xy-plane); plane B, longitudinal and aligned with the cutting guide (yz-plane) (Figure 5).

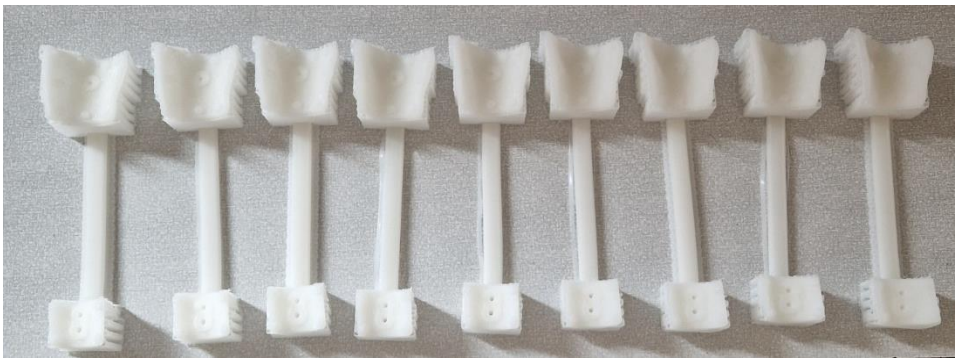

**Figure 3.** Some of the specimens after printing, annealing, and support removal, ready for scanning.

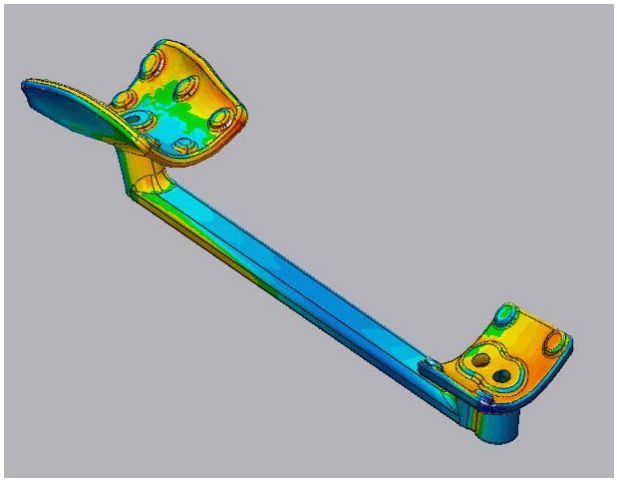

**Figure 4.** 3D distance map of the stl model of one of the specimens compared to the original CAD for 3D deformation assessment.

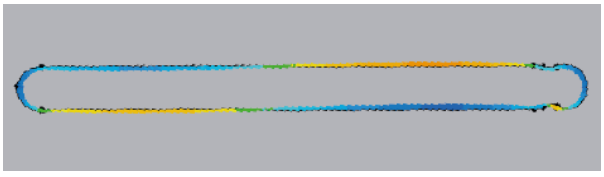

 doi:10.20944/preprints202511.0067.v1



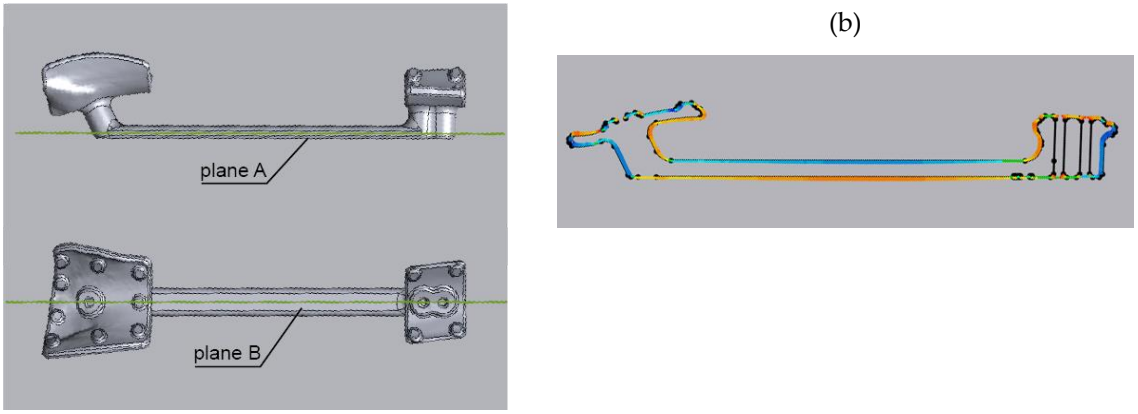


(**a**) (**b**)

**Figure 5.** (**a**) 3D model showing the planes used for 2D deformation cross-sectional analysis; Illustrative example of the 2D cross-sectional comparison on plane A (**b**) and plane B (**c**): orange/yellow areas indicate positive deformation relative to the original model, while blue/light blue areas indicate negative deformation, calculated as the distance measured along the normals.

### *2.5. Data Analysis*

The analysed parameters included 3D deformation, deformation on Plane A, and deformation on Plane B, all assessed with respect to the original model. For each parameter, the standard deviation was evaluated to ensure the detection of actual variations that could not be captured by the mean value alone.

Given the screening objective of identifying the factors influencing deformation, an exploratory data analysis was first conducted, followed by an ANOVA (Analysis of Variance) limited to main effects. A p-value below 0.05 was considered indicative of statistical significance.

## 3. Results

### *3.1. $2^4$ Factorial Design Analysis*

With four factors varied at two levels, the collected data (Table 5) were initially analyzed using a $2^4$ factorial design without replicates, given the screening objective of the experiment. To identify the main effects influencing the responses, half-normal probability plots of the effect estimates were constructed (Figure 6), and the contribution rates of each term to the responses are summarized in Table 6.

**Table 5.** Design matrix of the experiments, including randomized run order and corresponding response values (in mm). 3d_dev: standard deviation of the 3D distance map comparison; plA_dev: standard deviation of the 2D comparison performed on plane A; plB_dev: standard deviation of the 2D comparison performed on plane B.

| Standard Order | Run Order | A | B | C | D | 3d_dev | plA_dev | plB_dev |
|---|---|---|---|---|---|---|---|---|
| 1 | 1 | - | - | - | - | 0,63 | 0,35 | 0,70 |
| 2 | 7 | + | - | - | - | 0,47 | 0,21 | 0,60 |
| 3 | 10 | - | + | - | - | 0,48 | 0,34 | 0,44 |
| 4 | 6 | + | + | - | - | 0,65 | 0,39 | 0,51 |
| 5 | 15 | - | - | + | - | 0,59 | 0,24 | 0,60 |
| 6 | 11 | + | - | + | - | 0,55 | 0,31 | 0,60 |
| 7 | 5 | - | + | + | - | 0,56 | 0,48 | 0,65 |
| 8 | 4 | + | + | + | - | 0,54 | 0,43 | 0,61 |
| 9 | 9 | - | - | - | + | 0,82 | 0,35 | 0,75 |

 doi:10.20944/preprints202511.0067.v1



| | | | | | | | | |
|---|---|---|---|---|---|---|---|---|
| 10 | 3 | + | - | - | + | 0,80 | 0,36 | 0,77 |
| 11 | 8 | - | + | - | + | 0,61 | 0,48 | 0,70 |
| 12 | 13 | + | + | - | + | 0,53 | 0,48 | 0,58 |
| 13 | 14 | - | - | + | + | 0,65 | 0,37 | 0,75 |
| 14 | 12 | + | - | + | + | 0,84 | 0,29 | 0,70 |
| 15 | 16 | - | + | + | + | 0,57 | 0,34 | 0,62 |
| 16 | 2 | + | + | + | + | 0,83 | 0,54 | 1,05 |

**Table 6.** Contribution (%) of the main terms for each response (The remaining percentage values corresponded to interaction effects, which were excluded from this preliminary investigation).

| | 3d_dev | plA_dev | plB_dev |
|---|---|---|---|
| (A) Raft thickness (layers) | 2,57 | 0,17 | **1,68*** |
| (B) Infill pattern angle (°) | 9,09 | 50,92 | 3,04 |
| (C) First-layer pattern | **0,41*** | **0,14*** | 7,78 |
| (D) Fan speed (%) | 36,72 | 10,97 | 30,53 |

*Values in bold highlight the factors with the lowest contribution.

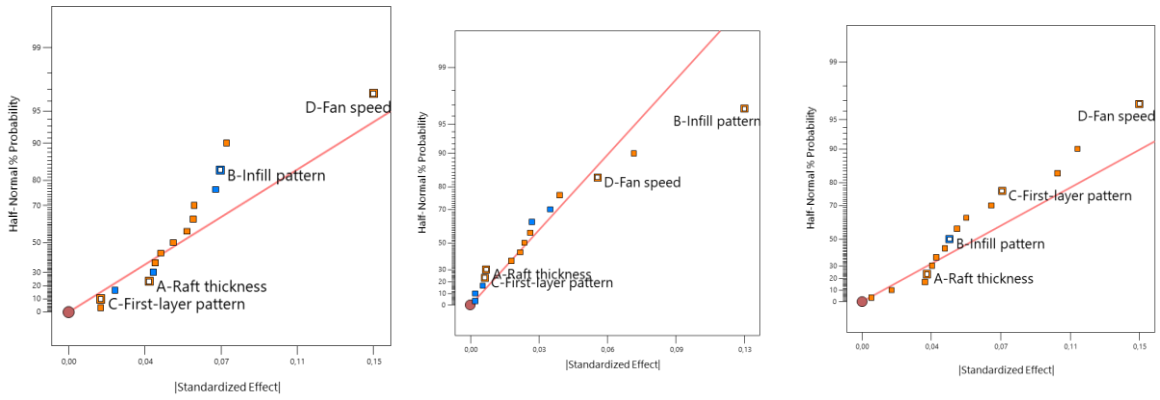


(**a**) (**b**) (**c**)

**Figure 6.** Half-normal probability plots of the effects for the $2^4$ factorial design for each response variable (positive effect in orange, negative effect in blue), with the four factors highlighted. (**a**) Plots for the 3d_dev response; (**b**) Plots for the plA_dev response; (**c**) Plots for the plB_dev response.

The plots indicate that fan speed has the greatest impact on both the overall 3D deformation and the deformation observed on cross-sectional Plane B. In contrast, deformation on Plane A appears to be primarily influenced by the infill pattern. Raft thickness and first-layer pattern appear to have negligible influence on the responses.

5. For the 3D deformation, the lowest value of standard deviation was 0,47 mm, while the highest was 0,83 mm, which corresponds respectively to standard order specimen n.2 (raft thickness layer=6; infill pattern degree=45, first layer pattern=M and fan speed percentage=25) and n.14 (raft thickness layer=6; infill pattern degree=45, first layer pattern=H and fan speed percentage=100);
6. For the deformation on plane A, the lowest value of standard deviation was 0,21 mm, while the highest was 0,54 mm, which corresponds respectively to standard order n.2 (raft thickness layer=6; infill pattern degree=45, first layer pattern=M and fan speed percentage=25) and n.16 (raft thickness layer=6; infill pattern degree=90, first layer pattern=H and fan speed percentage=100);
7. For the deformation on plane B, the lowest value of standard deviation was 0,44 mm, while the highest was 1,05 mm, which corresponds respectively to standard order n.3 (raft thickness layer=0; infill pattern degree=90, first layer pattern=M and fan speed percentage=25) and n.16

 doi:10.20944/preprints202511.0067.v1



(raft thickness layer=6; infill pattern degree=90, first layer pattern=H and fan speed percentage=100).

These data show that plane B experienced the highest deformation, indicating that this plane is more sensitive to shape modifications. Both the 3D deformation and plane A exhibited the lowest deformation in specimen no. 2 from the standard order, which aligns with the initial assumption derived from graphical analysis: lower fan speed and a lower infill percentage result in reduced deformation. The highest standard deviation for 3D deformation was observed in specimen no. 14, which also had a higher fan speed—this agrees with the overall findings. The highest deformation value for both plane A and plane B was found in specimen no. 16, which is consistent with the graphical analysis, showing a higher infill percentage for plane A and a higher fan speed for plane B. Plane B exhibited its lowest deformation in specimen no. 3, which was printed with a lower fan speed.

Overall, the highest deformation in visible in plane B. The specimens are illustrated in Figure 7 and 8.

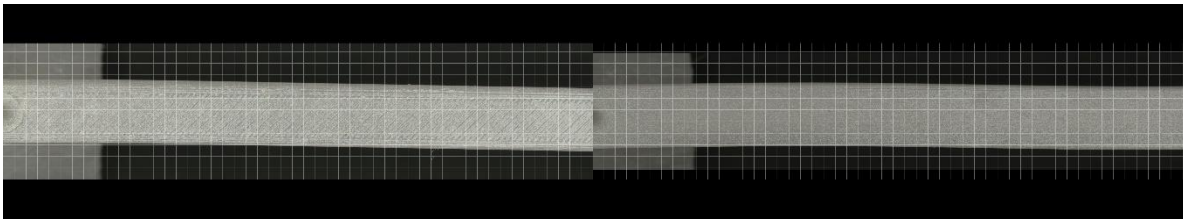

(**a**) (**b**)

**Figure 7.** Specimen no. 2 (a), which exhibited the lowest deformation in both the overall 3D deformation and on Plane A, and specimen no. 3 (b), which showed the lowest deformation on Plane B. A 2 × 2 mm grid was overlaid to better highlight the deformation.

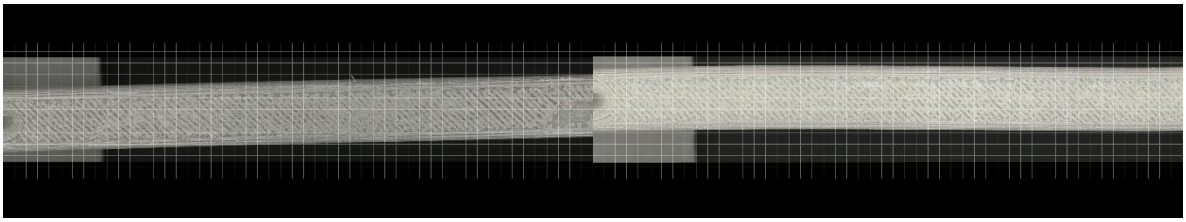

(**a**) (**b**)

**Figure 8.** Specimen no. 14 (a), which exhibited the highest overall 3D deformation, and specimen no. 16 (b), which showed the highest deformation on both Plane A and Plane B. A 2 × 2 mm grid was overlaid to better highlight the deformation.

### *3.2. Projection into a $2^3$ Design*

Since the first-layer pattern appeared to be non-significant and showed the lowest contribution percentage across most responses, it was excluded from further analysis. As a result, the original $2^4$ design was projected into a $2^3$ factorial design with two replicates, allowing for the estimation of experimental error and enabling the application of ANOVA. The three factors considered were raft thickness, infill pattern orientation, and cooling fan speed (Table 7).

**Table 7.** Values of the high and low levels for each new factor.

| | **Factor** | **Levels** | |
|---|---|---|---|
| | | **Low (-)** | **High (+)** |
| Raft thickness (layers) | A | 0 | 6 |
| Infill pattern (°) | B | 45° | 90° |
| Fan speed (%) | C | 25% | 100% |

 doi:10.20944/preprints202511.0067.v1



The revised half-normal probability plot for the $2^3$ design validated the results obtained in the previous analysis (Figure 9). The main factors with a positive effect on deformation are the infill pattern orientation and the fan speed. This indicates that higher infill orientation angles and increased fan speed lead to greater deformation.

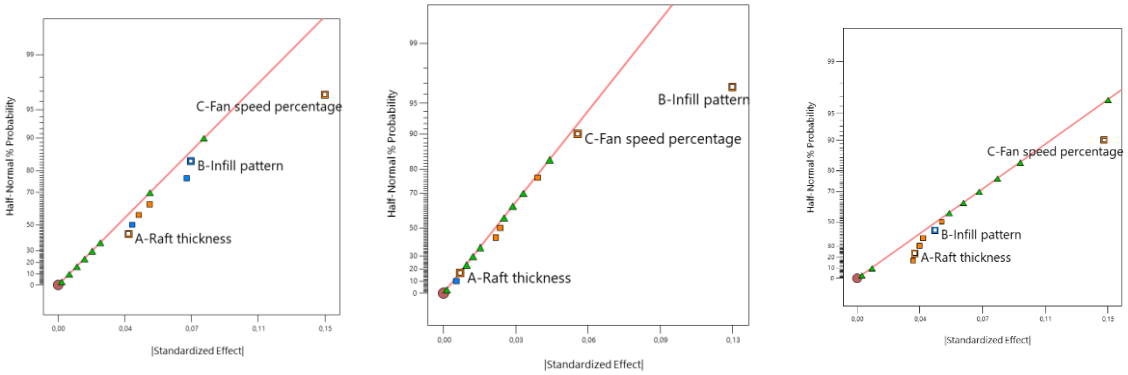


**Figure 9.** Half-normal probability plots of the effects for the $2^3$ factorial design for each response variable (positive effect in orange, negative effect in blue), with the three factors highlighted. (**a**) Plots for the 3d_dev response; (**b**) Plots for the plA_dev response; (**c**) Plots for the plB_dev response.

The ANOVA results show that fan speed and infill pattern have significant main effects, respectively on the 3D deformation and the 2D deformation of plane A. In contrast, plane B does not show any significant factors. No interaction effects are significant (Tables 8–10).

**Table 8.** ANOVA analysis for the 3d_dev response.

| | Sum of Squares | df | Mean Square | F-value | p-value |
|---|---|---|---|---|---|
| **Model** | 0,1581 | 7 | 0,0226 | 2,37 | **0,1245** |
| A-Raft thickness | 0,0060 | 1 | 0,0060 | 0,6330 | 0,4492 |
| B-Infill pattern | 0,0213 | 1 | 0,0213 | 2,24 | 0,1730 |
| C-Fan speed percentage | 0,0860 | 1 | 0,0860 | 9,04 | **0,0169*** |
| AB | 0,0079 | 1 | 0,0079 | 0,8269 | 0,3897 |
| AC | 0,0102 | 1 | 0,0102 | 1,07 | 0,3312 |
| BC | 0,0200 | 1 | 0,0200 | 2,11 | 0,1848 |
| ABC | 0,0067 | 1 | 0,0067 | 0,7008 | 0,4268 |
| **Pure Error** | 0,0762 | 8 | 0,0095 | | |
| **Cor Total** | 0,2343 | 15 | | | |

*Values in bold with an asterisk highlight the factors that are statistically significant ($p < 0.05$).

**Table 9.** ANOVA analysis for the plA_dev response.

| | Sum of Squares | df | Mean Square | F-value | p-value |
|---|---|---|---|---|---|
| **Model** | 0,0889 | 7 | 0,0127 | 2,83 | **0,0843** |
| A-Raft thickness | 0,0002 | 1 | 0,0002 | 0,0470 | 0,8338 |
| B-Infill pattern | 0,0636 | 1 | 0,0636 | 14,15 | **0,0055*** |
| C-Fan speed percentage | 0,0137 | 1 | 0,0137 | 3,05 | 0,1189 |
| AB | 0,0068 | 1 | 0,0068 | 1,51 | 0,2547 |
| AC | 0,0021 | 1 | 0,0021 | 0,4655 | 0,5143 |
| BC | 0,0001 | 1 | 0,0001 | 0,0283 | 0,8706 |
| ABC | 0,0025 | 1 | 0,0025 | 0,5483 | 0,4802 |
| **Pure Error** | 0,0359 | 8 | 0,0045 | | |
| **Cor Total** | 0,1248 | 15 | | | |

*Values in bold with an asterisk highlight the factors that are statistically significant ($p < 0.05$).

 doi:10.20944/preprints202511.0067.v1



**Table 10.** ANOVA analysis for the plB_dev response.

| | Sum of Squares | df | Mean Square | F-value | p-value |
|---|---|---|---|---|---|
| **Model** | 0,1228 | 7 | 0,0175 | 0,9183 | **0,5382** |
| A-Raft thickness | 0,0046 | 1 | 0,0046 | 0,2417 | 0,6362 |
| B-Infill pattern | 0,0084 | 1 | 0,0084 | 0,4393 | 0,5261 |
| C-Fan speed percentage | 0,0841 | 1 | 0,0841 | 4,40 | 0,0691 |
| AB | 0,0099 | 1 | 0,0099 | 0,5168 | 0,4927 |
| AC | 0,0054 | 1 | 0,0054 | 0,2813 | 0,6103 |
| BC | 0,0060 | 1 | 0,0060 | 0,3165 | 0,5891 |
| ABC | 0,0044 | 1 | 0,0044 | 0,2281 | 0,6457 |
| **Pure Error** | 0,1528 | 8 | 0,0191 | | |
| **Cor Total** | 0,2756 | 15 | | | |

*Values in bold with an asterisk highlight the factors that are statistically significant ($p < 0.05$).

The graphical representation of the main effects shows that lower deformation is achieved with the fan speed set at its lowest value (25%) and with a 45° infill pattern (Figure 10).

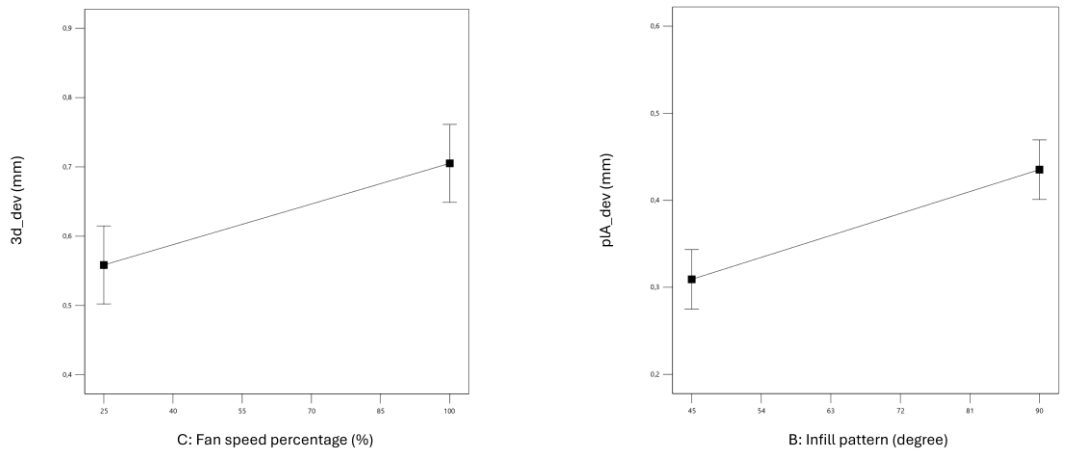


(**a**) (**b**)

**Figure 10. (a)** Main effect plot for the fan speed for 3d_dev response; **(b)** Main effect plot for the infill pattern for plA_dev response.

However, the ANOVA for the 3D_dev response yielded a non-significant model p-value. When the analysis was recalculated excluding raft thickness, which appeared non-significant, the resulting simplified model became significant for both overall 3D deformation and deformation on Plane A. The lack-of-fit test was non-significant, indicating a good representation of the data, while Plane B remained non-significant (Tables 11–13)

**Table 11.** Recalculated ANOVA without the raft-thickness factor for the 3D_dev response.

| | Sum of Squares | df | Mean Square | F-value | p-value |
|---|---|---|---|---|---|
| **Model** | 0,1274 | 3 | 0,0425 | 4,77 | **0,0206*** |
| B-Infill pattern | 0,0213 | 1 | 0,0213 | 2,39 | 0,1479 |
| C-Fan speed percentage | 0,0860 | 1 | 0,0860 | 9,66 | **0,0091*** |

 doi:10.20944/preprints202511.0067.v1



| | | | | | |
|---|---|---|---|---|---|
| BC | 0,0200 | 1 | 0,0200 | 2,25 | 0,1595 |
| Residual | 0,1069 | 12 | 0,0089 | | |
| Lack of Fit | 0,0308 | 4 | 0,0077 | 0,8077 | **0,5537** |
| **Pure Error** | 0,0762 | 8 | 0,0095 | | |
| **Cor Total** | 0,2343 | 15 | | | |

*Values in bold with an asterisk highlight the factors that are statistically significant ($p < 0.05$).

**Table 12.** Recalculated ANOVA without the raft-thickness factor for the plA_dev response.

| | Sum of Squares | df | Mean Square | F-value | p-value |
|---|---|---|---|---|---|
| **Model** | 0,0774 | 3 | 0,0258 | 6,52 | **0,0073*** |
| B-Infill pattern | 0,0636 | 1 | 0,0636 | 16,07 | **0,0017*** |
| C-Fan speed percentage | 0,0137 | 1 | 0,0137 | 3,46 | 0,0874 |
| BC | 0,0001 | 1 | 0,0001 | 0,0321 | 0,8607 |
| Residual | 0,0475 | 12 | 0,0040 | | |
| Lack of Fit | 0,0115 | 4 | 0,0029 | 0,6416 | **0,6479** |
| **Pure Error** | 0,0359 | 8 | 0,0045 | | |
| **Cor Total** | 0,1248 | 15 | | | |

*Values in bold with an asterisk highlight the factors that are statistically significant ($p < 0.05$).

**Table 13.** Recalculated ANOVA without the raft-thickness factor for the plB_dev response.

| | Sum of Squares | df | Mean Square | F-value | p-value |
|---|---|---|---|---|---|
| **Model** | 0,0986 | 3 | 0,0329 | 2,23 | **0,1376** |
| B-Infill pattern | 0,0084 | 1 | 0,0084 | 0,5688 | 0,4653 |
| C-Fan speed percentage | 0,0841 | 1 | 0,0841 | 5,70 | 0,0343 |
| BC | 0,0060 | 1 | 0,0060 | 0,4098 | 0,5341 |
| Residual | 0,1770 | 12 | 0,0148 | | |
| Lack of Fit | 0,0242 | 4 | 0,0061 | 0,3170 | **0,8590** |
| **Pure Error** | 0,1528 | 8 | 0,0191 | | |
| **Cor Total** | 0,2756 | 15 | | | |

*Values in bold with an asterisk highlight the factors that are statistically significant ($p < 0.05$).

The analysis indicates that only the main effects, infill pattern and fan speed, contribute significantly to the overall 3D deformation and to deformation on Plane A, whereas interaction terms do not provide meaningful explanatory power and can therefore be excluded from the model. Deformation on Plane B is not significantly explained by these factors.

Finally, from the results and the graphs (Figures 11 and 12), it can be stated with confidence that minimizing overall 3D deformation requires setting the fan speed to its lowest value during printing (even though it is not significant according to the results for Plane A). The effect of the infill pattern, however, appears less straightforward. For deformation on Plane A, the lowest values were observed at 45°, whereas the 3D_dev response showed the lowest deformation at 90°. This apparent contradiction may be explained by the alignment of the 90° linear infill with the vertical connecting rod, which creates longer continuous lines on Plane A. These lines accumulate greater tension during annealing, as their orientation favours stress concentration along the rod. Moreover, during

 doi:10.20944/preprints202511.0067.v1



deposition, the longer lines, spanning the entire length of the rod, may cool more rapidly when laid adjacent to one another, since neighboring lines are already cold, thereby inducing lateral adhesion stresses reflected on Plane A (xy-plane). Altogether, these findings suggest that the observed differences between 45° and 90° infill orientations result from a complex interplay of geometric alignment, thermal gradients, and stress release during annealing.

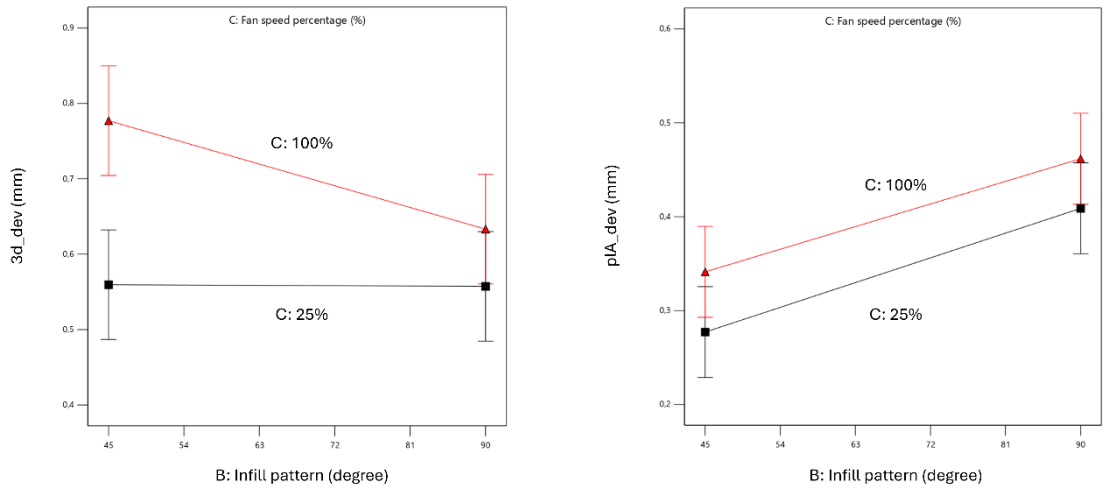


(**a**) (**b**)

**Figure 11. (a)** Main effect plot of fan speed for the 3D_dev response; (**b**) Main effect plot of infill pattern for the plA_dev response. The red line represents high fan speed (100%), while the black line represents low fan speed (25%).

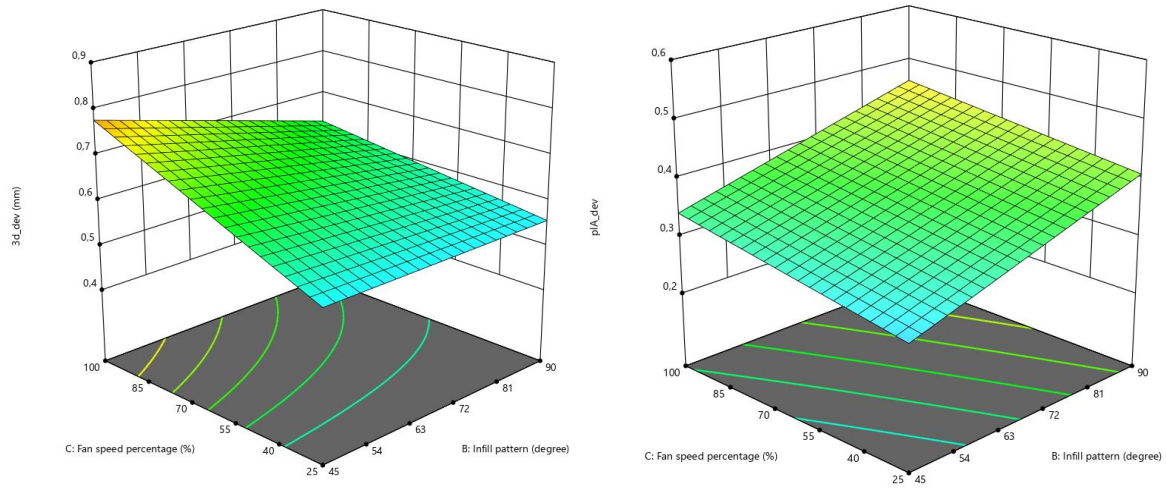


(**a**) (**b**)

**Figure 12. (a)** 3D response surface plot for the 3D_dev response; (**b**) 3D response surface plot of infill pattern for the plA_dev response. Yellow/red areas indicate higher deformation at that point, whereas light blue/blue areas indicate lower deformation.

While the most robust evidence concerns the reduction of overall 3D deformation at lower fan speeds, the present dataset was likely insufficient to capture the full complexity of the response. This indicates the need for further research with additional factor levels to account for possible non-linear effects, greater statistical power, and more replicates to reduce model noise. Moreover, other parameters not investigated here (such as infill geometry rather than orientation, the number of walls, etc.) may also play an important role. Therefore, even though the current results are significant, they should be regarded as a starting point for future studies aimed at process optimization.

 doi:10.20944/preprints202511.0067.v1



## 4. Discussion

Literature clearly shows that the mechanical properties of FDM parts are strongly influenced by process parameters such as printing speed, extrusion and build plate temperatures, infill density and pattern, layer height, and layer width. Optimizing these variables is essential to achieve the desired mechanical performance, dimensional accuracy, and overall part quality [27]. Furthermore, the strength of 3D-printed components is inherently anisotropic, with its extent largely determined by the selected process parameters [28–31].

In FDM, the plastic is rapidly heated, extruded, and cooled in contact with previously deposited layers. Because of its low thermal conductivity, this rapid heating and cooling generate internal stresses and cause layer shrinkage. The process is also prone to weak interlayer adhesion and voids, which reduce part quality and may require post-processing to improve mechanical properties [16,17]. Among the available post-processing techniques for FDM parts, annealing is one of the most effective. By increasing crystallinity, it reduces internal stresses, improves interlayer adhesion, and enhances mechanical properties [32–35]. Its effects vary with polymer type: in ABS, quality improves mainly through material reflow and gap filling, while in PLA, flexural strength increases with higher crystallinity, depending on annealing temperature and heating/cooling cycles [36,37]. Annealing can alter the dimensional tolerances of FDM parts, so shrinkage and expansion must be considered during design [18].

Steam sterilization (121–134 °C) is a key requirement in medical applications, being the most widely used method for sterilization worldwide, but standard PLA softens above its glass transition and degrades under heat and moisture, making autoclaving challenging. Still, studies show that with appropriate conditioning, such as material selection, geometric design, and pre-annealing, PLA can better withstand autoclaving, with reduced dimensional change and acceptable strength retention.

Tarragó et al. studied heat-induced deformation in FDM PLA 3D fracture biomodels subjected to autoclave sterilization. They analysed specimens with different infill percentages and found that sterilization reduced the total area of the biomodels. The 25% infill protocol showed the highest efficiency, with a mean deformity of 0.41 mm (SD 0.09; 95% CI 0.34–0.47; $p < 0.01$). The smallest area loss was also observed in this group (mean 0.29 $cm^2$, SD 0.83), resulting in no statistically significant difference between pre- and post-sterilization volumes also evaluating sterilization effectiveness [38]. While they reported the mean deformation across the whole area after superimposing pre- and post-sterilization models, and our study instead used the standard deviation of the distance map, both metrics are conceptually aligned. Our lowest value for 3D deformation (0.47 mm SD) is therefore of similar magnitude, supporting the consistency of these findings across methods. It should be noted, however, that their assessment was performed directly after sterilization, without considering the effect of prior annealing, which was the focus of our work. Similarly, Boursier et al. analysed autoclave sterilization on FDM-printed PLA bone models, focusing on the effect of temperature, and reported minimal deformation values [39].

Ferretti et al. demonstrated that optimal performance was achieved with previously annealed HTPLA, confirming the need for accurate control of heating and cooling times to ensure material stability at high temperatures. PLA showed results above expectations, making it a valid low-cost option and a promising alternative for disposable medical tools requiring only a single heat cycle [20].

Cerezo et al. investigated annealing-induced deformation in ABS and PLA, with and without a ceramic powder mould, and found that it was most pronounced along the main length, although the mould reduced the effect in both materials. The mould proved more effective in ABS (amorphous) than in PLA (semi-crystalline), which showed less deformation overall and no degradation [40]. Similarly, in our study the maximum deformation deviation was observed on Plane B, despite the absence of significant factors, while Plane A showed the highest deformation at 90° infill orientation, consistent with the lengthwise direction of the part.

Wijnbergen et al. investigated FDM with tough PLA for low-cost prosthetic sockets and tested different annealing methods. They found that sand annealing produced the least deformation, while

 doi:10.20944/preprints202511.0067.v1



oven annealing of vertically placed rings caused the largest dimensional changes but also the greatest improvement in mechanical properties [41]. These findings indicate that the position of the part during annealing is an additional parameter affecting deformation, an aspect not considered in our study, but potentially relevant for future investigations alongside printing parameters and infill orientation.

### *4.1. Limitations*

This study, while providing valuable insights, also presents some limitations. First of all, not all the possible printing parameters that can be defined during slicing were investigated, due to the incredibly high number of possible parameters, which also differ between slicing software. This is the reason why only a few parameters, considered the most impactful by their nature, were selected.

A further limitation is that dimensional variation was assessed on a single custom cutting guide with a total length of 142 mm. Given the high level of personalization, it is difficult to establish a standardized protocol applicable to all models, as could be done with generic or regular geometries. Consequently, the results apply specifically to this design, with its overall length and the defined dimensions of the connection rod.

Moreover, all measurements were taken after annealing and before sterilization. In our experience, no relevant deformations have been observed after sterilization when annealing was performed, at least none sufficient to compromise the usability of the guides. For this reason, the effect of sterilization was not included in the present analysis. Measuring only after sterilization would not have clarified whether any deformation was due to annealing or to sterilization and would have required two separate measurement phases, one for each treatment, which was excessively time-consuming. Nonetheless, further studies incorporating sterilization are warranted to empirically confirm the absence of additional deformations following this process.

Moreover, measurements were not taken immediately after printing, as the study focused on deformations relative to the original model. The aim was to assess the effect of printing parameters on the dimensional stability of a large-scale object, regardless of the printer's baseline accuracy.

The factorial design was intended as a screening experiment rather than a full optimization. Only two levels per factor were tested, assuming linear relationships between factors and responses, which is an acceptable simplification for preliminary purposes, although higher-order interactions or non-linear effects may exist but were not captured. In addition, no replicates were initially performed due to the large number of specimens and the time required for each test, which prevented the estimation of experimental error and may have introduced some inaccuracy. However, the design was subsequently reduced to a $2^3$ factorial with at least one replicate, allowing for error estimation. Further studies with more levels and additional replications are needed to obtain more precise results and move towards parameter optimization..

## 5. Conclusions

This study demonstrated that printing parameters strongly influence the dimensional stability of 3D-printed FDM HTPLA PSIs subjected to annealing before sterilization. A fan speed of 25% and an infill orientation of 45° for overall 3D deformation, and 90° for Plane A, emerged as the main influencing factors, although their effects were not consistent across all planes, likely due to the high anisotropy of the printed parts.

Overall 3D deformation and Plane A were significantly affected, whereas Plane B showed the greatest deviation but was not explained by the tested factors, underscoring the complexity of anisotropic behavior. Despite limitations related to the number of parameters, absence of replicates in the initial design, and the use of a single guide geometry, this work provides a first step toward understanding and predicting deformations in long, PSIs. Further studies with more factor levels, replications, and inclusion of sterilization are needed to improve predictive models and support process optimization for clinical use.

 doi:10.20944/preprints202511.0067.v1



**Author Contributions:** Conceptualization, G.C.M., ; methodology, A.M.; software, G.A. and P.P.; validation, A.M. and P.P.; formal analysis, G.A.; investigation, G.C.M.; resources, G.R., L.F; data curation, G.C.M.; writing—original draft preparation, G.C.M. and A.M.; writing—review and editing, G.T. and P.P; visualization, G.A.; supervision, G.T. and G.R.; project administration, G.R., L.F.; funding acquisition, G.T. and L.F.

**Funding:** This research received no external funding.

**Institutional Review Board Statement:** Not applicable.

**Informed Consent Statement:** Not applicable.

**Data Availability Statement:** Data are available from the authors upon reasonable request.

**Conflicts of Interest:** The authors declare no conflicts of interest.

## Abbreviations

The following abbreviations are used in this manuscript:

| | |
|---|---|
| CAD | Computer-Aided Design |
| AM | Additive Manufacturing |
| STL | Stereolithography |
| FDM | Fused Deposition modelling |
| ABS | Acrylonitrile-Butadiene-Styrene |
| PLA | Polylactic Acid |
| HTPLA | High-Temperature Polylactic Acid |
| ANOVA | Analysis of Variance |

## References

8. Sarkar, Jayanta. Computer Aided Design : A Conceptual Approach. 2015, 713.
9. Vannier, M.W.; Marsh, J.L.; Warren, J.O. Three Dimensional CT Reconstruction Images for Craniofacial Surgical Planning and Evaluation. *Radiology* 1984, *150*, 179–184, doi:10.1148/RADIOLOGY.150.1.6689758.
10. Hull, C. On Stereolithography. *Virtual Phys Prototyp* 2012, *7*, 177, doi:10.1080/17452759.2012.723409.
11. Kruth, J.P.; Leu, M.C.; Nakagawa, T. Progress in Additive Manufacturing and Rapid Prototyping. *CIRP Annals* 1998, *47*, 525–540, doi:10.1016/S0007-8506(07)63240-5.
12. Karkun, M.S.; Dharmalingam, S. 3D Printing Technology in Aerospace Industry – A Review. *International Journal of Aviation, Aeronautics, and Aerospace* 2022, *9*, 4, doi:https://doi.org/10.15394/ijaaa.2022.1708.
13. Blakey-Milner, B.; Gradl, P.; Snedden, G.; Brooks, M.; Pitot, J.; Lopez, E.; Leary, M.; Berto, F.; du Plessis, A. Metal Additive Manufacturing in Aerospace: A Review. *Mater Des* 2021, *209*, 110008, doi:10.1016/J.MATDES.2021.110008.
14. Mohanavel, V.; Ashraff Ali, K.S.; Ranganathan, K.; Allen Jeffrey, J.; Ravikumar, M.M.; Rajkumar, S. The Roles and Applications of Additive Manufacturing in the Aerospace and Automobile Sector. *Mater Today Proc* 2021, *47*, 405–409, doi:10.1016/J.MATPR.2021.04.596.
15. Khajavi, S.H.; Mandolini, M. Additive Manufacturing in the Clothing Industry: Towards Sustainable New Business Models. *Applied Sciences 2021, Vol. 11, Page 8994* 2021, *11*, 8994, doi:10.3390/APP11198994.
16. Javaid, Mohd.; Haleem, A. Additive Manufacturing Applications in Medical Cases: A Literature Based Review. *Alexandria Journal of Medicine* 2018, *54*, 411–422, doi:10.1016/J.AJME.2017.09.003.
17. Ferretti, P.; Fusari, E.; Alessandri, G.; Freddi, M.; Francia, D. Stress-Based Lattice Structure Design for a Motorbike Application. *F1000Research 2023 11:1162* 2023, *11*, 1162, doi:10.12688/f1000research.125184.2.
18. Cano-Vicent, A.; Tambuwala, M.M.; Hassan, S.S.; Barh, D.; Aljabali, A.A.A.; Birkett, M.; Arjunan, A.; Serrano-Aroca, Á. Fused Deposition Modelling: Current Status, Methodology, Applications and Future Prospects. *Addit Manuf* 2021, *47*, 102378, doi:10.1016/J.ADDMA.2021.102378.
19. Shahrubudin, N.; Lee, T.C.; Ramlan, R. An Overview on 3D Printing Technology: Technological, Materials, and Applications. *Procedia Manuf* 2019, *35*, 1286–1296, doi:10.1016/J.PROMFG.2019.06.089.

20. Doshi, M.; Mahale, A.; Singh, S.K.; Deshmukh, S. Printing Parameters and Materials Affecting Mechanical Properties of FDM-3D Printed Parts: Perspective and Prospects. *Mater Today Proc* 2022, *50*, 2269–2275, doi:10.1016/J.MATPR.2021.10.003.
21. Jariwala, S.H.; Lewis, G.S.; Bushman, Z.J.; Adair, J.H.; Donahue, H.J. 3D Printing of Personalized Artificial Bone Scaffolds. *3D Print Addit Manuf* 2015, *2*, 56–64, doi:10.1089/3DP.2015.0001.
22. Hao, Y.; Luo, D.; Wu, J.; Wang, L.; Xie, K.; Yan, M.; Dai, K. A Novel Revision System for Complex Pelvic Defects Utilizing 3D-Printed Custom Prosthesis. *J Orthop Translat* 2021, *31*, 102–109, doi:10.1016/j.jot.2021.09.006.
23. Vanaei, H.R.; Khelladi, S.; Deligant, M.; Shirinbayan, M.; Tcharkhtchi, A. Numerical Prediction for Temperature Profile of Parts Manufactured Using Fused Filament Fabrication. *J Manuf Process* 2022, *76*, 548–558, doi:10.1016/J.JMAPRO.2022.02.042.
24. Tao, Y.; Kong, F.; Li, Z.; Zhang, J.; Zhao, X.; Yin, Q.; Xing, D.; Li, P. A Review on Voids of 3D Printed Parts by Fused Filament Fabrication. *Journal of Materials Research and Technology* 2021, *15*, 4860–4879, doi:10.1016/J.JMRT.2021.10.108.
25. Butt, J.; Bhaskar, R. Investigating the Effects of Annealing on the Mechanical Properties of FFF-Printed Thermoplastics. *Journal of Manufacturing and Materials Processing 2020, Vol. 4, Page 38* 2020, *4*, 38, doi:10.3390/JMMP4020038.
26. Donnici, G.; Freddi, M.; Liverani, A. RSM Applied to Lattice Patterns for Stiffness Optimization. *Rapid Prototyp J* 2024, *30*, 344–355, doi:10.1108/RPJ-03-2024-0134/FULL/PDF.
27. Frizziero, L.; Santi, G.M.; Leon-Cardenas, C.; Ferretti, P.; Sali, M.; Gianese, F.; Crescentini, N.; Donnici, G.; Liverani, A.; Trisolino, G.; et al. Heat Sterilization Effects on Polymeric, FDM-Optimized Orthopedic Cutting Guide for Surgical Procedures. *J Funct Biomater* 2021, *12*, doi:10.3390/jfb12040063.
28. Frizziero, L.; Santi, G.M.; Leon-Cardenas, C.; Donnici, G.; Liverani, A.; Napolitano, F.; Papaleo, P.; Pagliari, C.; Antonioli, D.; Stallone, S.; et al. An Innovative and Cost-Advantage Cad Solution for Cubitus Varus Surgical Planning in Children. *Applied Sciences (Switzerland)* 2021, *11*, doi:10.3390/app11094057.
29. Ferretti, P.; Leon-Cardenas, C.; Sali, M.; Santi, G.M.; Gianese, F.; Donnici, G. Material Characterization Analysis of PLA & HTPLA FDM-Sourced Elements with Annealing Procedure and Optimized Printing Parameters. *Proceedings of the International Conference on Industrial Engineering and Operations Management* 2021, 1410–1420.
30. Leon-Cardenas, C.; Ferretti, P.; Sali, M.; Santi, G.M.; Gianese, F.; Crescentini, N.; Frizziero, L.; Donnici, G.; Liverani, A.; Trisolino, G.; et al. FDM-Sourced Shinbone Cutting Guide in Polylactic Acid-Based Polymers: Heat Sterilization Effects on Part Quality. *Proceedings of the International Conference on Industrial Engineering and Operations Management* 2021, 764–772.
31. Vishnoi, M.; Mamatha, T.G.; Singh, M.; -, al; Shorinov, O.; Dolmatov, A.; Polyviany, S.; Hamouti, L.; El Farissi, O.; Laouardi, M. Experimental Study of the Effect of Different 3D Printing Parameters on Tensile Strength, Using Artificial Neural Network. *Mater Res Express* 2024, *11*, 035505, doi:10.1088/2053-1591/AD3465.
32. Alzyod, H.; Borbas, L.; Ficzere, P. Rapid Prediction and Optimization of the Impact of Printing Parameters on the Residual Stress of FDM-ABS Parts Using L27 Orthogonal Array Design and FEA. *Mater Today Proc* 2023, *93*, 583–588, doi:10.1016/J.MATPR.2023.02.213.
33. Alzyod, H.; Ficzere, P. Correlation Between Printing Parameters and Residual Stress in Additive Manufacturing: A Numerical Simulation Approach. *Production Engineering Archives* 2023, *29*, 279–287, doi:10.30657/PEA.2023.29.32.
34. Jaisingh Sheoran, A.; Kumar, H. Fused Deposition Modeling Process Parameters Optimization and Effect on Mechanical Properties and Part Quality: Review and Reflection on Present Research. *Mater Today Proc* 2020, *21*, 1659–1672, doi:10.1016/J.MATPR.2019.11.296.
35. Qamar Tanveer, M.; Mishra, G.; Mishra, S.; Sharma, R. Effect of Infill Pattern and Infill Density on Mechanical Behaviour of FDM 3D Printed Parts- a Current Review. *Mater Today Proc* 2022, *62*, 100–108, doi:10.1016/J.MATPR.2022.02.310.

36. Agarwal, K.M.; Shubham, P.; Bhatia, D.; Sharma, P.; Vaid, H.; Vajpeyi, R. Analyzing the Impact of Print Parameters on Dimensional Variation of ABS Specimens Printed Using Fused Deposition Modelling (FDM). *Sensors International* 2022, *3*, 100149, doi:10.1016/J.SINTL.2021.100149.
37. Rodríguez-Panes, A.; Claver, J.; Camacho, A.M. The Influence of Manufacturing Parameters on the Mechanical Behaviour of PLA and ABS Pieces Manufactured by FDM: A Comparative Analysis. *Materials 2018, Vol. 11, Page 1333* 2018, *11*, 1333, doi:10.3390/MA11081333.
38. Popescu, D.; Zapciu, A.; Amza, C.; Baciu, F.; Marinescu, R. FDM Process Parameters Influence over the Mechanical Properties of Polymer Specimens: A Review. *Polym Test* 2018, *69*, 157–166, doi:10.1016/J.POLYMERTESTING.2018.05.020.
39. Ravoori, D.; Salvi, S.; Prajapati, H.; Qasaimeh, M.; Adnan, A.; Jain, A. Void Reduction in Fused Filament Fabrication (FFF) through in Situ Nozzle-Integrated Compression Rolling of Deposited Filaments. *Virtual Phys Prototyp* 2021, *16*, 146–159, doi:10.1080/17452759.2021.1890986.
40. Kim, H.-C.; Kim, D.-Y.; Lee, J.-E.; Park, K. Improvement of Mechanical Properties and Surface Finish of 3d-Printed Polylactic Acid Parts by Constrained Remelting. *Adv Mater Lett* 2017, *8*, 1199–1203, doi:10.5185/AMLETT.2017.1686.
41. Lee, S.K.; Kim, Y.R.; Kim, S.H.; Kim, J.H. Investigation of the Internal Stress Relaxation in FDM 3D Printing : Annealing Conditions. *Journal of the Korean Society of Manufacturing Process Engineers* 2018, *17*, 130–136, doi:10.14775/KSMPE.2018.17.4.130.
42. Liao, Y.; Liu, C.; Coppola, B.; Barra, G.; Di Maio, L.; Incarnato, L.; Lafdi, K. Effect of Porosity and Crystallinity on 3D Printed PLA Properties. *Polymers 2019, Vol. 11, Page 1487* 2019, *11*, 1487, doi:10.3390/POLYM11091487.
43. Wach, R.A.; Wolszczak, P.; Adamus-Wlodarczyk, A. Enhancement of Mechanical Properties of FDM-PLA Parts via Thermal Annealing. *Macromol Mater Eng* 2018, *303*, 1800169, doi:10.1002/MAME.201800169.
44. Singh, S.; Singh, M.; Prakash, C.; Gupta, M.K.; Mia, M.; Singh, R. Optimization and Reliability Analysis to Improve Surface Quality and Mechanical Characteristics of Heat-Treated Fused Filament Fabricated Parts. *International Journal of Advanced Manufacturing Technology* 2019, *102*, 1521–1536, doi:10.1007/S00170-018-03276-8/METRICS.
45. Ferràs-Tarragó, J.; Sabalza-Baztán, O.; Sahuquillo-Arce, J.M.; Angulo-Sánchez, M.Á.; De-La-Calva Ceinos, C.; Amaya-Valero, J.V.; Baixauli-García, F. Autoclave Sterilization of an In-House 3D-Printed Polylactic Acid Piece: Biological Safety and Heat-Induced Deformation. *European Journal of Trauma and Emergency Surgery* 2022, *48*, 3901–3910, doi:10.1007/S00068-021-01672-6/FIGURES/6.
46. Boursier, J.F.; Fournet, A.; Bassanino, J.; Manassero, M.; Bedu, A.S.; Leperlier, D. Reproducibility, Accuracy and Effect of Autoclave Sterilization on a Thermoplastic Three-Dimensional Model Printed by a Desktop Fused Deposition Modelling Three-Dimensional Printer. *Vet Comp Orthop Traumatol* 2018, *31*, 422–430, doi:10.1055/S-0038-1668113.
47. Lluch-Cerezo, J.; Meseguer, M.D.; García-Manrique, J.A.; Benavente, R. Influence of Thermal Annealing Temperatures on Powder Mould Effectiveness to Avoid Deformations in ABS and PLA 3D-Printed Parts. *Polymers (Basel)* 2022, *14*, doi:10.3390/POLYM14132607.
48. Wijnbergen, D.C.; van der Stelt, M.; Verhamme, L.M. The Effect of Annealing on Deformation and Mechanical Strength of Tough PLA and Its Application in 3D Printed Prosthetic Sockets. *Rapid Prototyp J* 2021, *27*, 81–89, doi:10.1108/RPJ-04-2021-0090/FULL/PDF.